Human Molecular Genetics, 2016, Vol. 25, No. 21 4686–4702

doi: 10.1093/hmg/ddw296
Advance Access Publication Date: 29 August 2016
Original Article

ORIGINAL ARTICLE

Pathogenic inflammation in the CNS of mice carrying human *PLP1* mutations

Janos Groh[1,*], Hana C. Friedman[2], Nadiya Orel[3], Chi Wang Ip[1], Stefan Fischer[1], Irene Spahn[1], Erik Schäffner[1], Michaela Hörner[1], David Stadler[1], Mathias Buttmann[4], Csanad Varallyay[5], László Solymosi[5], Michael Sendtner[3], Alan C. Peterson[2] and Rudolf Martini[1]

[1]Department of Neurology, Section of Developmental Neurobiology, University Hospital Wuerzburg, D-97080 Wuerzburg, Germany, [2]Laboratory of Developmental Biology, Ludmer Research and Training Building, McGill University, Montreal, QC, Canada, [3]Institute of Clinical Neurobiology, University of Wuerzburg, Wuerzburg, Germany, [4]Department of Neurology, Multiple Sclerosis and Neuroimmunology, University Hospital Wuerzburg, Wuerzburg, Germany and [5]Division of Neuroradiology, University Hospital Wuerzburg, Wuerzburg, Germany

*To whom correspondence should be addressed at: Janos Groh, Department of Neurology, Section of Developmental Neurobiology, University Hospital Wuerzburg, Josef-Schneider-Str. 11, D-97080 Wuerzburg, Germany. Tel: +49-931-201-23778; Fax: +49-931-201-23645; Email: groh_j@ukw.de

Abstract

Progressive forms of multiple sclerosis lead to chronic disability, substantial decline in quality of life and reduced longevity. It is often suggested that they occur independently of inflammation. Here we investigated the disease progression in mouse models carrying *PLP1* point mutations previously found in patients displaying clinical features of multiple sclerosis. These mouse models show loss-of-function of *PLP1* associated with neuroinflammation; the latter leading to clinically relevant axonal degeneration, neuronal loss and brain atrophy as demonstrated by inactivation of the recombination activating gene 1. Moreover, these pathological hallmarks were substantially amplified when we attenuated immune regulation by inactivation of the programmed cell death-1 gene. Our observations support the view that primary oligodendroglial abnormalities can evoke pathogenically relevant neuroinflammation that drives neurodegeneration, as observed in some forms of multiple sclerosis but also in other, genetically-mediated neurodegenerative disorders of the human nervous system. As many potent immunomodulatory drugs have emerged during the last years, it is tempting to consider immunomodulation as a treatment option not only for multiple sclerosis, but also for so far non-treatable, genetically-mediated disorders of the nervous system accompanied by pathogenic neuroinflammation.

Introduction

Neuroinflammation-induced neural damage is a common feature of immune-related CNS disorders, paradigmatically represented by the relapsing-remitting forms of multiple sclerosis (RRMS) which usually respond to immunomodulatory therapy (1,2). In contrast to the treatable RRMS, the chronic-progressive subforms of multiple sclerosis (PMS) are often considered to occur independently of inflammation, as they are usually poorly responsive to established immune-modulatory therapeutic approaches (3,4). According to the 'inside-out' concept of

Received: July 8, 2016. **Revised:** August 12, 2016. **Accepted:** August 21, 2016

multiple sclerosis patho-aetiology, an unknown, primary degenerative disorder targets the myelin-oligodendrocyte complex inducing neuroinflammation in the relapsing-remitting phase, but is no longer active during the PMS stage which is then defined by the pure neurodegenerative disease course (5,6). However, it is conceivable that inflammatory reactions are still pathogenic drivers in PMS, but are inaccessible to many of the immune-modulatory drugs, partly due to an intact blood-brain barrier (BBB) (4–6).

Favouring the 'inside-out' model of neuroinflammation, recent years have seen emerging evidence that inflammatory reactions are associated with classical neurodegenerative disorders, such as Alzheimer's disease (7), Parkinson's disease (8), amyotrophic lateral sclerosis (9), prion disease (10) and stroke (11). Moreover, our group has shown that secondary inflammation amplifies the disease course and outcome in models for primarily genetically-mediated disorders of the CNS, such as distinct forms of neuronal ceroid lipofuscinoses (12,13) and *PLP1*-related leukodystrophies (14–19). Regarding the latter disease models targeting the myelin-oligodendrocyte complex, it is striking that distinct *PLP1* point mutations have been reported in humans to cause a clinical phenotype indistinguishable from primary progressive (20) or even steroid-responsive RRMS (21). Here, to further investigate the potential role of genetically-mediated neuroinflammation, we generated mouse models carrying the described *PLP1* point mutations and evaluated the mechanisms and impact of inflammation on axonal loss and neurodegeneration. We show that both mutations are pathogenic and evoke detrimental neuroinflammation: an observation that may explain the high degree of clinical similarity observed in PMS and some genetically-mediated disorders of the CNS, such as complicated hereditary spastic paraplegia. In summary, our study is focusing on neural damage as a potential cause for some forms of multiple sclerosis and neuroinflammation as a pathogenic driver in these disorders as well as in others primarily caused by identified CNS-related mutations.

Results

Generation of *PLPmut* mice

To generate mouse models carrying potentially pathogenic human point mutations described for the *PLP1* gene, we applied a strategy for integrating mutated 'W' (p.Leu30Arg) and 'G' (p.Arg137Trp) (20,21) or non-mutated human *PLP1* cDNA (Wt) in a controlled manner into the mouse genome (Supplementary Material, Fig. 1). Briefly, we introduced the point mutations by site-directed mutagenesis and subsequently integrated the human *PLP1* cDNAs with (*hPLPW*; *hPLPG*) or without (*hPLPWt*) the corresponding mutation into an entry vector containing a previously characterized *wmN1* enhancer to drive normal developmental and oligodendrocyte-specific expression (22). The constructs were transferred to a gateway destination vector enabling the controlled integration of the transgenes in single copy and known orientation adjacent to the murine X-linked *Hprt* locus (23) and mutant lines were generated from correctly targeted ES cells (24).

Full length transcription of the different *hPLP* constructs was confirmed by RT-PCR and sequencing of the cDNA products showed that the integrated point mutations were expressed (Supplementary Material, Fig. 2A). To prevent putative confounding effects of the additional endogenous murine *Plp1*, we cross-bred the generated transgenic lines with *Plp1* knockout mice (*PlpKo*) and selected for crossing over between the two X-linked loci (*Plp1*, *Hprt*).

We then determined the combined and individual relative expression levels of *PLP + DM20* mRNA at 2 months of age in the various mutant lines both before and after crossbreeding with *PlpKo* mice by semiquantitative real-time PCR (Supplementary Material, Fig. 2B and C). In comparison to *Wt* mice (with a detectable *PLP/DM20* ratio of approx. 1.8), mice expressing murine *Plp1* (*PlpWt*) and additionally non-mutated wild type human *PLP1* (*hPLPWt*) showed similar combined expression levels, while the *PLP/DM20* ratio was shifted towards *PLP* expression (approx. 3.0; Supplementary Material, Fig. 2B, C). Also, *PlpWt* mice expressing either of the mutant *hPLP1 cDNAs* (*hPLPW*; *hPLPG*) showed unchanged *PLP + DM20* levels, but the *PLP/DM20* ratio was even higher (4.5 and 4.9, respectively). As previously reported (25), *PLP + DM20* mRNA expression was strongly decreased, but not completely abolished in *PlpKo* mice due to the presence of a non-protein-coding transcript. All transgenic mice that were crossbred to *PlpKo* mice showed a complete lack of *DM20* mRNA expression, but the expression of *PLP1* mRNA was restored to Wt levels by the transgenes (Supplementary Material, Fig. 2B and C). Thus, the newly generated transgenic lines showed normal expression levels of *PLP1* mRNA, and human *PLP1* mRNA was the only open reading frame-containing transcript present in transgenic mice on a *PlpKo* background.

Investigation of PLP protein steady state levels by western blot analysis revealed comparable levels in *Wt* mice without the human transgene and *PlpWt* mice transgenic for either *hPLPWt*, *hPLPW* or *hPLPG* (Supplementary Material, Fig. 3A). Mice transgenic for human *PLP1* on the *PlpKo* background expectedly express solely human *PLP1* from the transgene and thus disclose the level of steady state levels of the human PLP Wt and mutant proteins (Supplementary Material, Fig. 3A). For instance, in *PlpKo* mice transgenic for *hPLPWt*, protein levels were reconstituted to approximately 50% of normal *Wt* mice. PLP protein steady state levels were also reconstituted by *hPLPW* or *hPLPG*, with reduced levels in the latter when compared to *hPLPWt/PlpKo* mice (Supplementary Material, Fig. 3A). Altogether, these experiments show that i) concomitant expression of murine and human *PLP1* (both mutant and non-mutant) does not lead to significant PLP overexpression and that ii) both wild type or mutant human PLP are synthesized in our mice and partially restore PLP levels when murine *Plp1* is inactivated.

By immunohistochemistry, PLP protein levels appeared reduced, but normally distributed in the optic nerves of *hPLPWt/PlpKo* compared with *Wt* mice (Supplementary Material, Fig. 3B). In contrast, PLP protein was retained in APC+ oligodendrocytic cell bodies and processes and strongly reduced in the myelin compartment of *hPLPW/PlpKo* and *hPLPG/PlpKo* mice, indicating that the mutations might result in disturbed myelin-directed trafficking. Of note, the densities of APC+ mature oligodendrocytes were similar in *Wt* and all transgenic mice, suggesting that altered protein levels in the respective mutants cannot be explained by major developmental alterations or cell death of oligodendrocytes (data not shown).

Neural damage in the CNS of *PLPmut* mice

Although axonal degeneration is a pivotal pathological hallmark in PMS eventually determining clinical outcome, we here first focus on myelin abnormalities as a direct structural measure for glial (*PLP1*)-related mutations. In semithin sections of optic nerves of all *PLPmut* mice (carrying mutant human *PLP1* on

murine *Plp1* knockout background, i.e. *hPLPW/PlpKo*; *hPLPG/PlpKo*, but also *PlpKo* mice) examined at 12 months of age, no prominent changes were visible except that the methylene blue-staining was consistently fainter than in *Wt* mice (Fig. 1A) possibly reflecting reduced membrane densities in myelin. Electron microscopy revealed a substantial perturbation of oligodendroglial myelin sheaths, with a high tendency of decompaction and myelin redundancies (Figs. 1B and 2A). Using higher magnifications, some myelin sheaths in *PLPmut* mice appeared normal, others showed a collapsed intraperiod line of high electron density instead of a double-stranded one. Additionally, robust myelin splitting and vanishing of intraperiod lines was visible, so that extended aspects of myelin appeared to consist of major dense lines solely, separated by electron-lucent aspects (Fig. 1C). Furthermore, axons with thin myelin sheaths or devoid of myelin were visible (Figs. 1D, 2A and D). Similar pathological alterations have been previously described in *PlpKo* mice (25–27).

Interestingly, in *hPLPWt/PlpWt* mice, myelin abnormalities were absent. In *hPLPWt/PlpKo* mice, distinct myelin splittings and collapsed intraperiod lines resembling those of *PLPmut* mice (Fig. 1C) and few thinly-/non-myelinated axons were visible (Figs. 1D and 2D). This is in line with the finding that only half of the normal *Wt* dose of PLP protein is synthesized in these

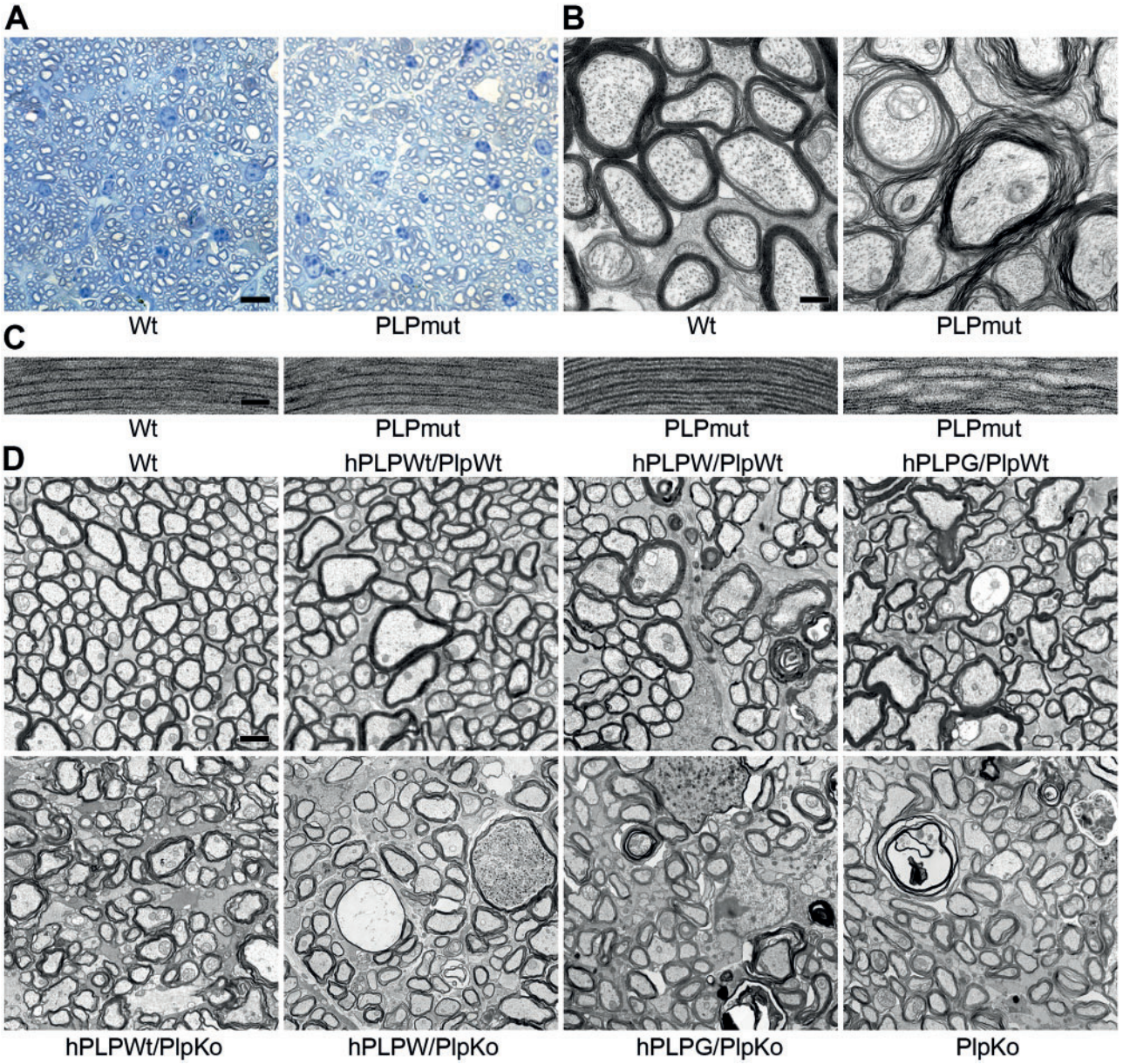

Figure 1. Ultrastructural CNS myelin alterations and neural pathology in *PLPmut* mice. (**A**) Representative semi-thin cross-sections of optic nerves from *Wt* and *PLPmut* mice stained with methylene blue. No prominent lesions were detected, but methylene blue staining was faint in *PLPmut* mice. Scale bar: 10 μm. (**B**) Representative electron micrographs of optic nerve sections from 2-month-old *Wt* and *PLPmut* mice. Myelin appeared decompacted and fanned out in *PLPmut* mice. Scale bar: 0.5 μm. (**C**) Higher magnification electron micrographs of *Wt* and *PLPmut* myelin. In *PLPmut* mice, some myelin sheaths appeared similar as in *Wt* mice (left), while others showed collapsed electron dense intraperiod lines (middle) or splitting and vanishing of intraperiod lines (right). Scale bar: 25 nm. (**D**) Representative electron micrographs of optic nerves from the various transgenic lines in comparison with *Wt* and *PlpKo* mice at 12 months of age. Thinly myelinated and demyelinated axons as well as axonal damage (spheroids and vacuoles) were detectable to different degrees. Scale bar: 2.5 μm.

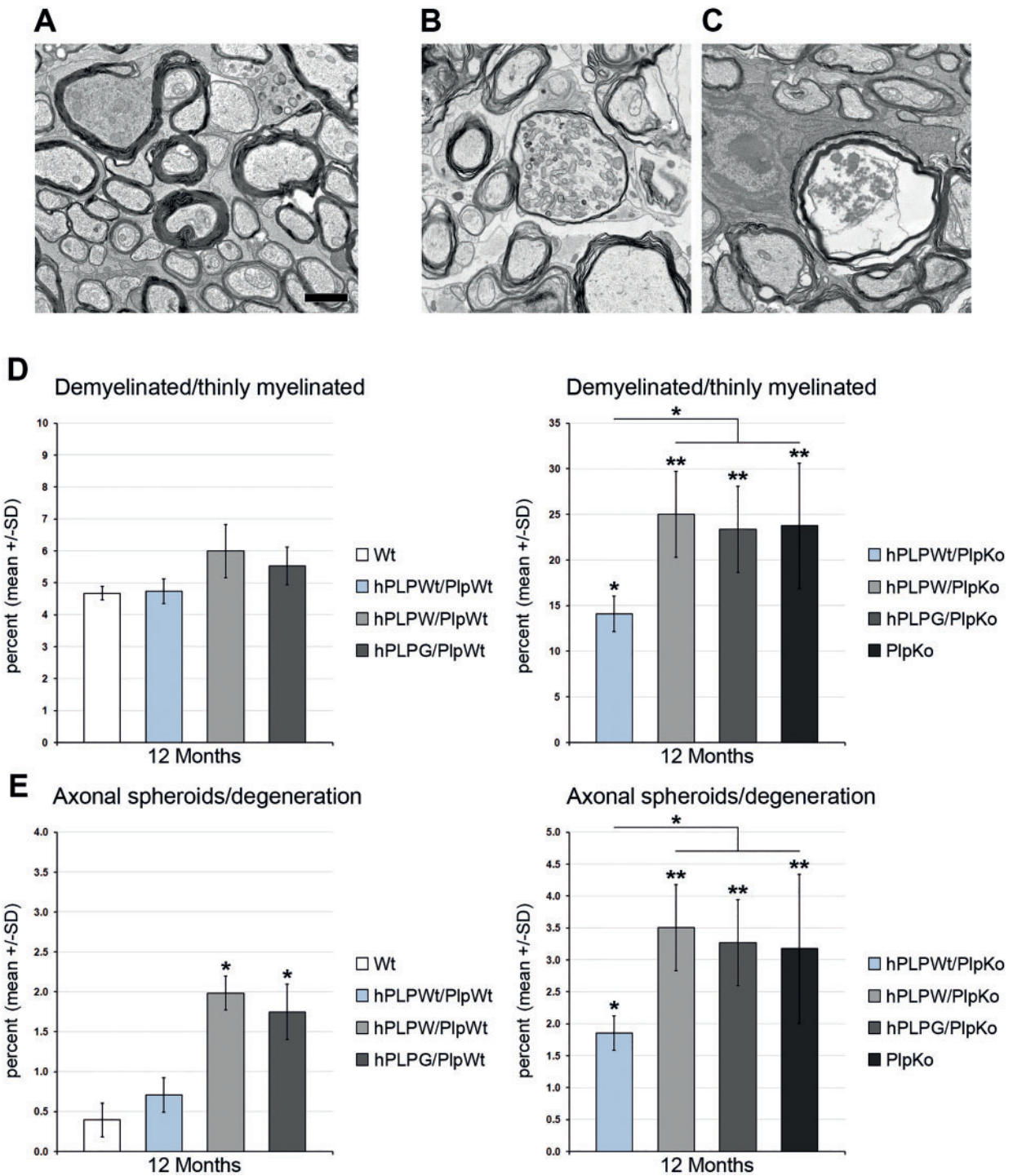

Figure 2. Impaired myelin integrity and axonal damage in the CNS of *PLPmut* mice. (**A**) Representative electron micrographs of optic nerves from 12-month-old *PLPmut* mice exemplifying thinly myelinated and demyelinated axons, (**B**) axonal spheroids and (**C**) degenerating axons with vacuole formation. Scale bar: 1.5 μm. (**D**) Morphometric quantification of demyelinated/thinly myelinated axons and (**E**) axonal spheroids/degeneration in optic nerves from the various transgenic lines in comparison with *Wt* and *PlpKo* mice at 12 months of age ($n = 4$ mice per group). Expression of *hPLPW* and *hPLPG* but not *hPLPWt* manifested in axonal damage without demyelination in *PlpWt* mice. Impaired myelin integrity and axonal damage in *PlpKo* mice were attenuated by *hPLPWt*, but not by *hPLPW* or *hPLPG*. Note the different scaling of the y-axes. Kruskal-Wallis test and Bonferroni-Holm correction. $^{*}P < 0.05$, $^{**}P < 0.01$.

mice (see Supplementary Material, Fig. 3B, right panel). Moreover, normal myelin in *hPLPWt/PlpWt* mice, but mild alterations in *hPLPW/PlpWt* and *hPLPG/PlpWt* mice reflect that both mouse and (non-functional or pathological) human PLP contribute to total protein levels of these mutants.

When shifting focus from myelin to axonal features, we found that axonal spheroids and vacuoles, both indicative of axonal degeneration, were absent in *hPLPWt/PlpWt* mice. However, these hallmarks of PMS were amply detectable in all other mutants (Figs. 1D, 2B and C).

Generally, in *hPLPW* and *hPLPG* genotypes, all pathological alterations (myelin and axonal) were more frequent in the absence of mouse PLP (*PlpKo*) (Figs. 1D, 2D and E) and there was no detectable difference in pathology between the *hPLPW/PlpWt* and *hPLPG/PlpWt* genotypes (Figs. 1D, 2D and E). Also, *hPLPW/PlpKo*, *hPLPG/PlpKo* and *PlpKo* mice strongly resembled each other with regard to their qualitative and quantitative pathological changes, detected by electron microscopy and implicating myelin and axonal features. In contrast, the *hPLPWt* transgene significantly attenuated pathological alterations in *PlpKo* mice by approximately 50%, reflecting the restored synthesis of functionally intact human PLP protein (Supplementary Material, Figs. 3A, Figs. 1D, 2D and E). Thus, both point mutations cause similar pathological alterations, either when the transgenes are co-expressed with normal endogenous mouse *Plp1* or in the absence of mouse *Plp1*. As the latter cases allowed us to interpret the effects of the respective mutation more accurately, we investigated these mutants in more detail. Ultrastructural myelin alterations were present at all investigated ages (2, 6, 12, 18 months). In contrast, the demyelinating and axonopathic features were barely detectable at 2 months of age (demyelinated/thinly myelinated axons in percent: *Wt* 4.6 +/- 1.4, *PLPmut* 7.8 +/- 2.9, not significant; for axonopathic features see also Supplementary Material, Fig. 10C and D), but manifested by 6 months of age and progressively increased with age (not shown). These findings are in line with reports arguing for normal myelin formation (25,26,28,29) followed by mild demyelination rather than delay in myelination from the onset (30), a presently unexplained discrepancy. The phenotypes observed here for *hPLPW/PlpKo* or *hPLPG/PlpKo* are most likely the result of a loss of PLP function due to the point mutations, as *hPLPWt* partially rescued the *PlpKo* phenotypes while the mutated *hPLPW* or *hPLPG* did not.

Accordingly, when axonal spheroids in optic nerves were quantified by SMI32 immunoreactivity in *hPLPW/PlpKo*, *hPLPG/PlpKo* and *PlpKo* mutants (Fig. 3A and C), axonal perturbation was already ongoing and increasing from postnatal month 6 to 18 (Fig. 3C) while in *hPLPWt/PlpKo* mice axonal perturbation was delayed and attenuated in comparison with the other *PLPmut* groups. Interestingly, loss of retinal ganglion cell somata occurred later than the axonal spheroid formation, again with delayed onset and attenuated severity in *hPLPWt/PlpKo* mice (Fig. 3B and D).

To supplement the analysis of retinal pathologies with a non-invasive technique, we analysed the retinae of living mice using OCT (Supplementary Material, Fig. 4A). *PLPmut* mice displayed a significantly reduced total retinal thickness due to thinning of the inner but not outer retina (Supplementary Material, Fig. 4B), solely due to a significant thinning of the NFL/GCL/IPL composite layer (Supplementary Material, Fig. 4C), corroborating the histological perturbation of retinal ganglion cells and their axons. Again the *hPLPW/PlpKo*, *hPLPG/PlpKo* and *PlpKo* mutants displayed similar degrees of degeneration, whereas *hPLPWt/PlpKo* mutants were less affected (Supplementary Material, Fig. 4D).

Analysis of living *PLPmut* mice by MRI at around 6 months of age revealed alterations in ventricle and corpus callosum-related signal intensity and size (Supplementary Material, Fig. 5A). At the advanced age (18 months) there was obvious CNS atrophy in *PLPmut* mice reflected by a reduction in overall forebrain and cerebellar size (Supplementary Material, Fig. 5B) and decreased brain and cerebellar weights, with *hPLPWt/PlpKo* mutants not significantly differing from Wt mice (Fig. 4A).

Accelerating Rotarod analysis revealed a reduced latency to fall off the rod by *hPLPW/PlpKo*, *hPLPG/PlpKo* and *PlpKo* mutants at postnatal month 15 and 18, while at 12 months there was no significant difference between *PLPmut* and *Wt* mice (Fig. 4B). At all ages, *hPLPWt/PlpKo* mutants showed a similar Rotarod performance (individual runs and cumulative) as *Wt* mice (Fig. 4B).

As potentially pathogenic cells, we investigated microglia/macrophages using CD11b as a pan marker and Sn as a marker for pro-inflammatory subtypes of these cells (13) (Supplementary Material, Fig. 6). Optic nerves of *Wt* mice revealed frequent, slim CD11b+ cells, whereas Sn+ cells were scarcely seen. In *hPLPWt/PlpKo* mutants, CD11b+ cells always showed similar values to *Wt* mice, while all *PLPmut* mice displayed a constant increase in numbers of these cells at all investigated ages (Supplementary Material, Fig. 6A and B). Numbers of activated Sn+ microglia/macrophages were mildly increased at postnatal month 12 in the *hPLPWt/PlpKo* mutants, but robustly in the *hPLPW/PlpKo*, *hPLPG/PlpKo* and *PlpKo* mutants (Supplementary Material, Fig. 6A–C). Similar data were obtained at 6 and 18 months (not shown). Cells of the adaptive immune system (CD8+ and CD4+ T-lymphocytes; Fig. 5) were also increased in number in all PLP mutants, with a mild increase in *hPLPWt/PlpKo* mutants and a robust increase in *PLPmut* mice.

Taken together, at all investigated ages *hPLPWt* ameliorated neural damage and inflammatory reactions in *PlpKo* mice whereas *hPLPW* or *hPLPG* had no effect, again arguing for loss of PLP function due to the introduced point mutations.

As we observed inflammatory features in the CNS of *PLPmut* mice, we investigated the functional integrity of the blood-brain-barrier (BBB), using immunohistochemically detected albumin extravasation as a marker (Supplementary Material, Fig. 7A). While none of the *Wt* and *PLPmut* mice displayed albumin extravasation, mice with an induced experimental autoimmune encephalomyelitis serving as positive controls for impaired BBB integrity displayed robust parenchymal albumin leakage around laminin+ microvessels. These findings were also confirmed using intravenously injected fluorescent dextran, which faithfully labelled retinal vessels in *PLPmut* mice by BAF imaging, as opposed to a diffuse vessel labeling in aged models for ceroid lipofuscinosis neuronal 3 (*Cln3*$^{-/-}$ mice), another positive control for BBB damage (Supplementary Material, Fig. 7B).

Pathogenic impact of inflammation in *PLPmut* mice

In order to investigate the impact of the adaptive immune system, we selected two approaches. First, we eliminated T- and B-lymphocytes by cross-breeding the *PLPmut* with *Rag1*$^{-/-}$ mice (31). Second, we amplified the impact of the adaptive immune system by cross-breeding the *PLPmut* mice with mice deficient in the immune-regulatory molecule PD-1. As expected, in *PLPmut/Rag1*$^{-/-}$ mice, CD8+ (Supplementary Material, Fig. 8A and B) and CD4+ (Supplementary Material, Fig. 8C) T-cells were absent, while the numbers of CD11b+ (Supplementary Material, Fig. 8A and D) and Sn+ (Supplementary Material, Fig. 8E) microglia/macrophages were decreased in comparison with *PLPmut* (*Rag1*$^{+/+}$) mice. An inverse regulation of CD8+, CD4+, CD11b+ and Sn+ cells was seen in *PLPmut/Pd-1*$^{-/-}$ mutants.

Histologically, inactivation of the adaptive immune system by RAG1-deficiency led to robustly attenuated formation of SMI32+ axonal spheroids (Fig. 6A and C) and a reduced loss of retinal ganglion cells (Fig. 6B and D). Longitudinal analysis by OCT revealed a diminished reduction of NFL/GCL/IPL thickness at all investigated ages in *PLPmut/Rag1*$^{-/-}$ mice (Supplementary Material, Fig. 9). By contrast, PD-1-deficiency led to an aggravation of the histological phenotypes in optic nerve and retina

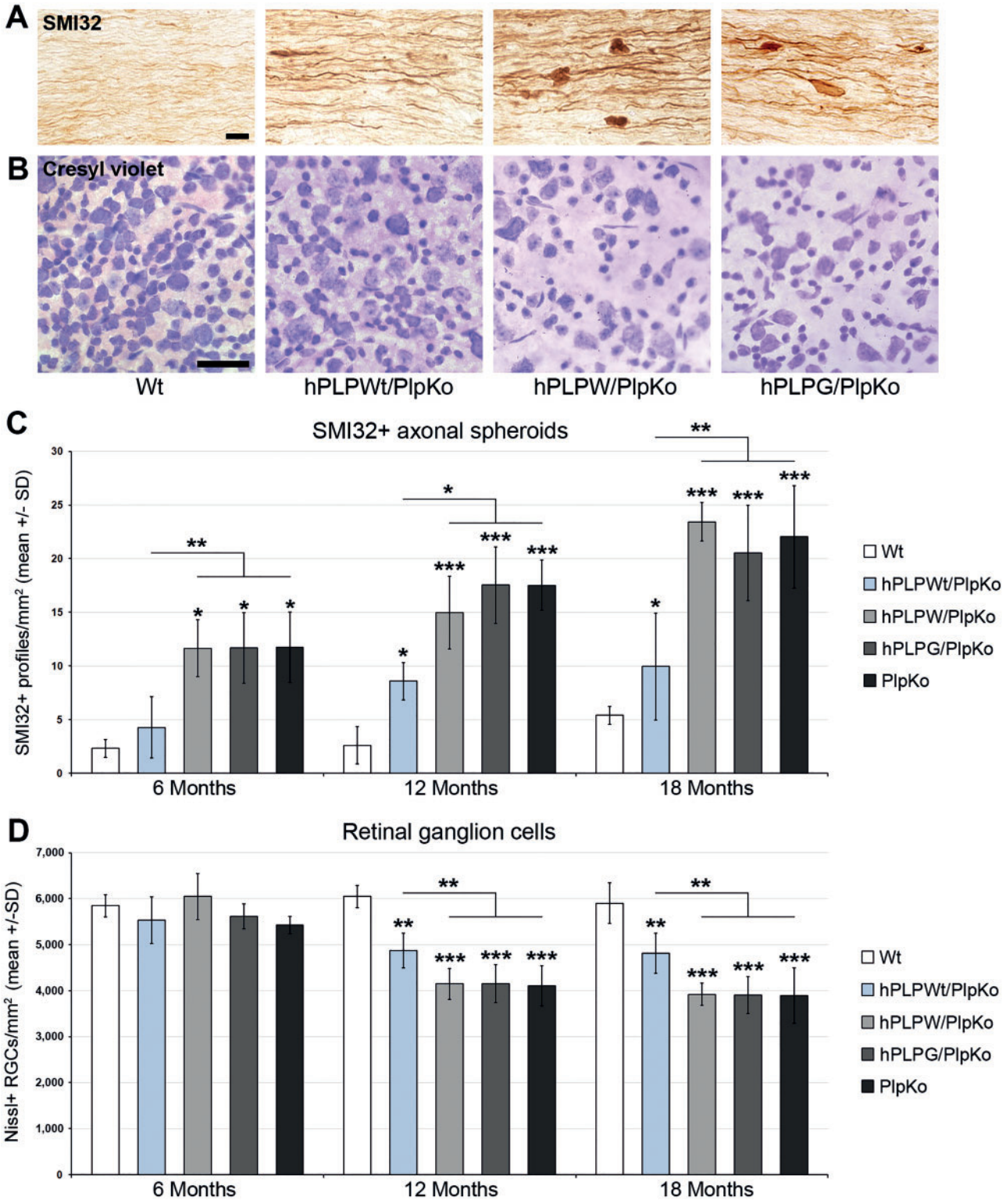

Figure 3. Progressive axonal degeneration and neuron loss in the CNS of *PLPmut* mice. (**A**) Representative light microscopic images of immunohistochemically labelled axonal spheroids using antibodies against non-phosphorylated neurofilaments (SMI32; brown precipitate) in longitudinal optic nerve sections and (**B**) cresyl violet stained retinal ganglion cells in flat mount preparations from 12-month-old Wt, *hPLPWt/PlpKo* and *PLPmut* mice. Scale bars: 30 μm. (**C**) Quantification of SMI32+ axonal spheroids and (**D**) Nissl+ RGCs in Wt, *hPLPWt/PlpKo* and *PLPmut* mice at 6, 12 and 18 months of age ($n = 5$ mice per group). Axonal degeneration and neuron loss in *PlpKo* mice were attenuated by *hPLPWt*, but not by *hPLPW* or *hPLPG*. One-way ANOVA and Tukey's *post hoc* tests. *$P < 0.05$, **$P < 0.01$, ***$P < 0.001$.

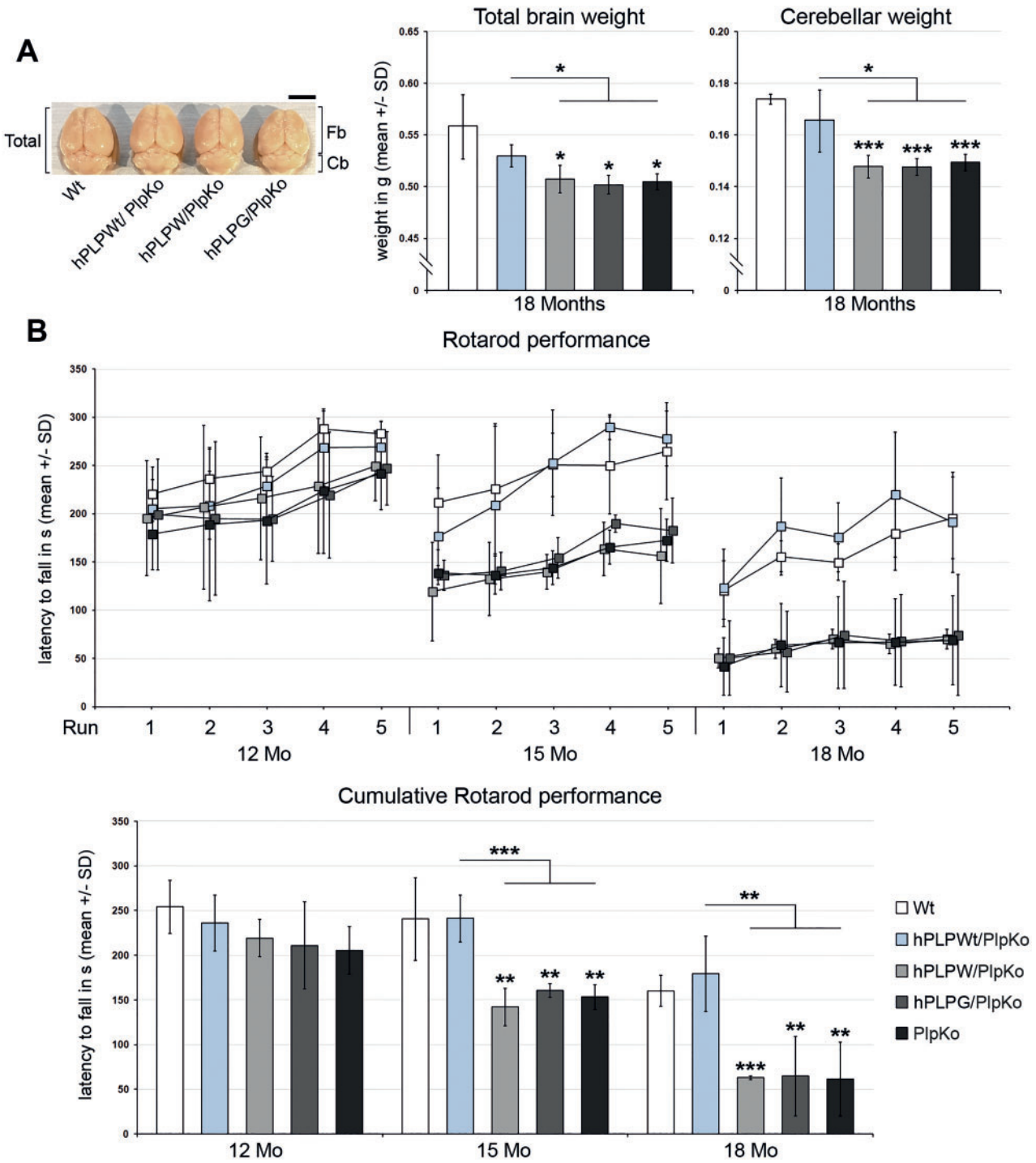

Figure 4. Brain atrophy and motor impairment in aged *PLPmut* mice. (**A**) Perfusion-fixed total brains or cerebelli from 18-month-old Wt, *hPLPWt/PlpKo* and *PLPmut* mice. Scale bar: 5 mm. Total brain or cerebellar atrophy in *PlpKo* mice was attenuated by *hPLPWt*, but not by *hPLPW* or *hPLPG* ($n = 5$ mice per group). (**B**) Longitudinal analysis of the Rotarod performance of Wt, *hPLPWt/PlpKo* and *PLPmut* mice at 12, 15 and 18 months of age showing individual runs or cumulative performance. Impairment of motor performance of 15- and 18-month-old *PlpKo* mice was ameliorated by *hPLPWt*, but not by *hPLPW* or *hPLPG* ($n = 5$ mice per group). One-way ANOVA and Tukey's *post hoc* tests. $^*P < 0.05$, $^{**}P < 0.01$, $^{***}P < 0.001$.

(Fig. 6) and more pronounced loss of the innermost retinal composite layer thickness, especially at advanced age (Supplementary Material, Fig. 9). Ultrastructural alterations in myelin architecture in *PLPmut* mice were not affected (not shown), but demyelination was attenuated by RAG1-deficiency and aggravated by PD-1-deficiency.

Total and cerebellar brain weights and Rotarod performance of *PLPmut* mice at 18 months of age also reflected attenuated or aggravated features, when adaptive immune reactions were genetically inactivated (*Rag1*$^{-/-}$) or enhanced (*Pd-1*$^{-/-}$), respectively (Fig. 7A and B). Some *PLPmut/Pd-1*$^{-/-}$ mice exhibited especially prominent pathological alterations (Fig. 7C) and began to show

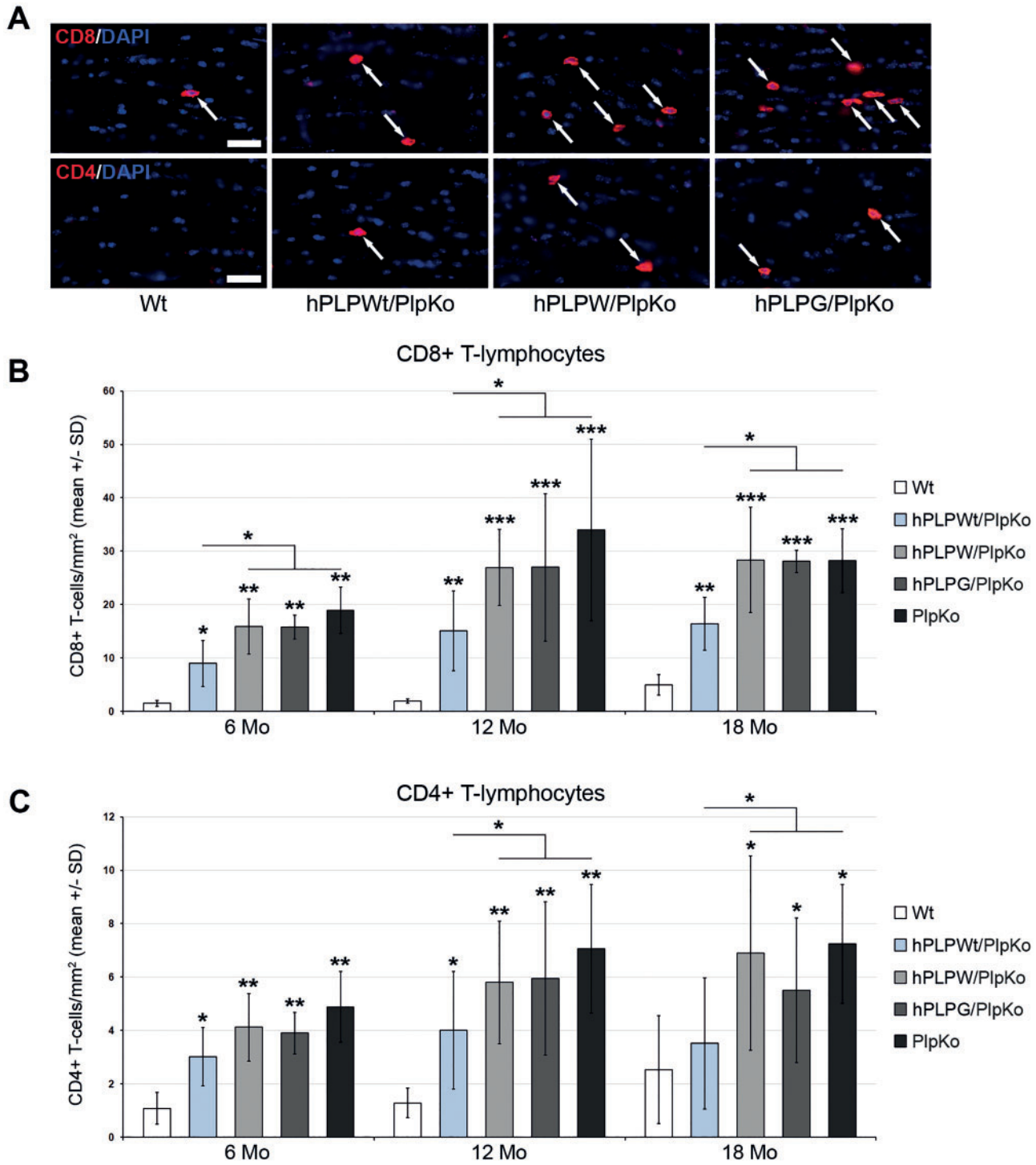

Figure 5. Increased numbers of T-lymphocytes in the CNS of *PLPmut* mice. (**A**) Representative fluorescence microscopic images of immunohistochemically labelled T-lymphocytes (arrows) using antibodies against CD8 (top) and CD4 (bottom) in longitudinal optic nerve sections from 12-month-old Wt, *hPLPWt/PlpKo* and *PLPmut* mice. Scale bars: 30 μm. (**B**) Quantification of CD8+ T-lymphocytes and (**C**) CD4+ T-lymphocytes at 6, 12 and 18 months. CD8+ T-cells strongly outnumbered CD4+ T-cells in the CNS of *PLPmut* mice (note the different scaling of the y-axes). Expansion of T-cell numbers in *PlpKo* mice was attenuated by *hPLPWt*, but not by *hPLPW* or *hPLPG* (n = 5 mice per group). One-way ANOVA and Tukey's *post hoc* tests. *$P < 0.05$, **$P < 0.01$, ***$P < 0.001$.

hind limb paralysis at 18 months of age (Fig. 7D). These affected mice were excluded from further investigations according to our internal ethical guidelines for animal experimentation and those recommended by the European Union.

Previous studies have identified juxtaparanodal domains as hotspots for axonal perturbation in distinct neurodegenerative models (12,13,18,32). When analysing longitudinal sections by electron microscopy at 6 months of age, also in *PLPmut* mice organelles and dense bodies accumulated preferentially at these domains eventually forming axonal spheroids (Supplementary Material, Fig. 10A). Both pro-inflammatory activated (Sn+) microglia/macrophages and CD8+ T-lymphocytes were

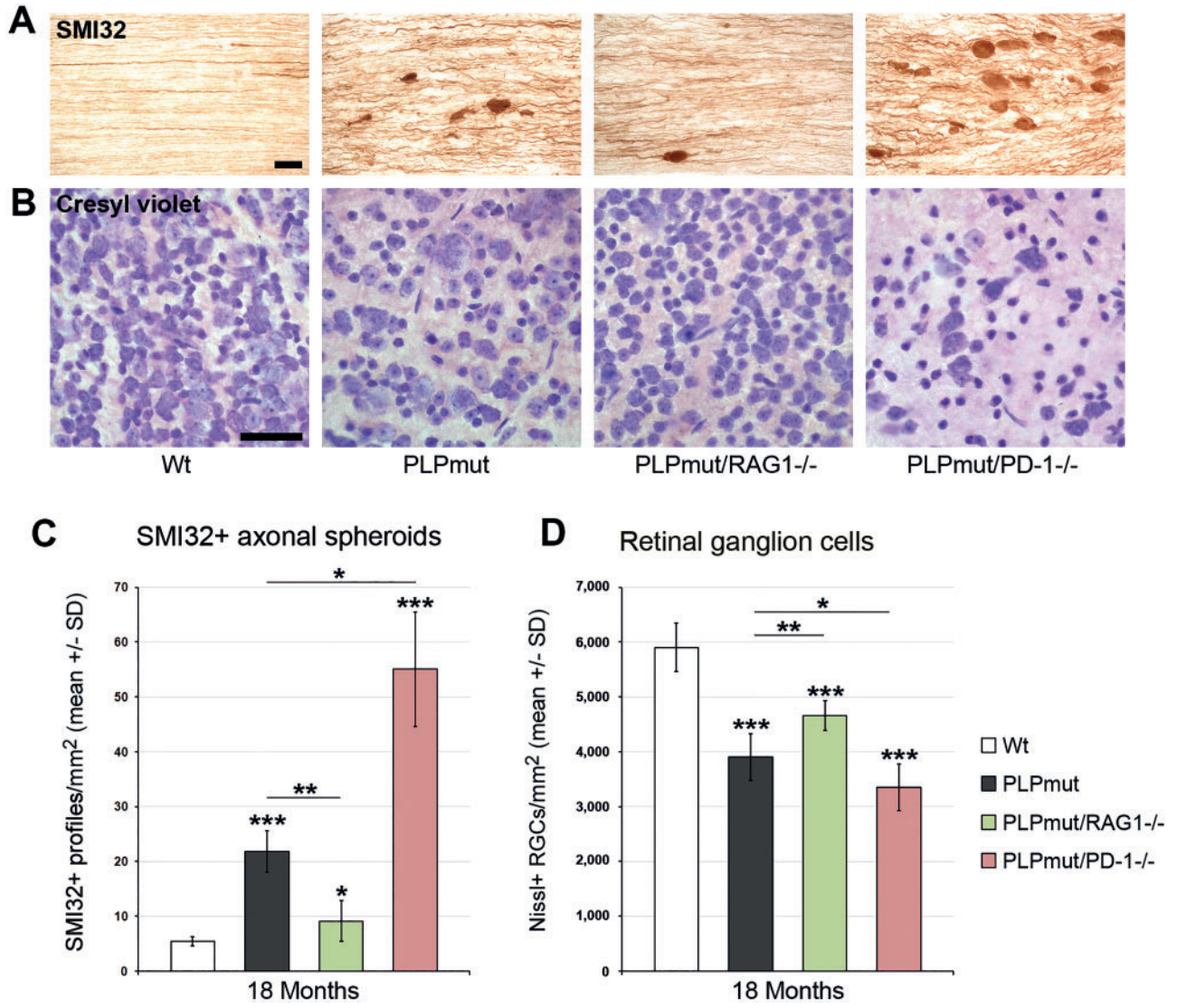

Figure 6. RAG1-deficiency attenuates and PD-1-deficiency aggravates neural damage in *PLPmut* mice. (**A**) Representative light microscopic images of immunohistochemically labelled SMI32+ axonal spheroids in longitudinal optic nerve sections (top) and (**B**) cresyl violet stained ganglion cells (bottom) in retinal flat mount preparations from 18-month-old Wt, *PLPmut*, *PLPmut/Rag1*$^{-/-}$ and *PLPmut/Pd-1*$^{-/-}$ mice. Scale bars: 30 μm. (**C**) Quantification of SMI32+ axonal spheroids and (**D**) Nissl+ RGCs in 18-month-old Wt, *PLPmut*, *PLPmut/Rag1*$^{-/-}$ and *PLPmut/Pd-1*$^{-/-}$ mice. Axonal damage and neuron loss were attenuated in *PLPmut/Rag1*$^{-/-}$ mice and increased in *PLPmut/Pd-1*$^{-/-}$ mice compared with *PLPmut* mice ($n = 5$ mice per group). One-way ANOVA and Tukey's *post hoc* tests. $^{*}P < 0.05$, $^{**}P < 0.01$, $^{***}P < 0.001$.

observed in direct association with small SMI32+ axonal spheroids (Supplementary Material, Fig. 10B). To test if inflammation also contributes to early functional axonal deficits we performed retrograde labeling experiments at 2 months of age when axonal spheroids are still rarely detectable by SMI32 reactivity or electron microscopy (Supplementary Material, Fig. 10C and D). Retrograde labeling of RGCs by FITC-CTB was quantified in flat mount preparations at 2 different time points after stereotactic injection into the superior colliculi. We detected delayed labeling suggesting attenuated efficacy, but not complete block of retrograde axonal transport in *PLPmut* mice (Fig. 8A and B). Similar to other pathological parameters, RAG1-deficiency restored the efficacy of retrograde labeling in *PLPmut* mice, while PD-1-deficiency strongly diminished retrograde labeling (Fig. 8A and B). At 2 months of age, CD8+ T-lymphocytes in the CNS of *PLPmut* mice were also preferentially associated with Caspr2+ juxtaparanodal axon domains and acquired a spindle-shaped form when attached to these regions as reflected by a lower form factor (Fig. 8C).

Discussion

We generated two mouse models for secondary neuroinflammation caused by glial (*PLP1*) gene mutations. We show that the resulting neuroinflammation is predominantly detrimental to axons and that attenuated immunoregulation exacerbates the primarily genetically caused disease. Most importantly, the same mutations generate a clinical scenario similar to multiple sclerosis in humans. These observations thus favour the possibility of an intrinsic origin of at least some multiple sclerosis forms (5,6).

The mouse models were designed in a way that the mutant *PLP1* transcripts were not overexpressed, which is reflected by their axonopathic instead of demyelinating phenotype (25,33).

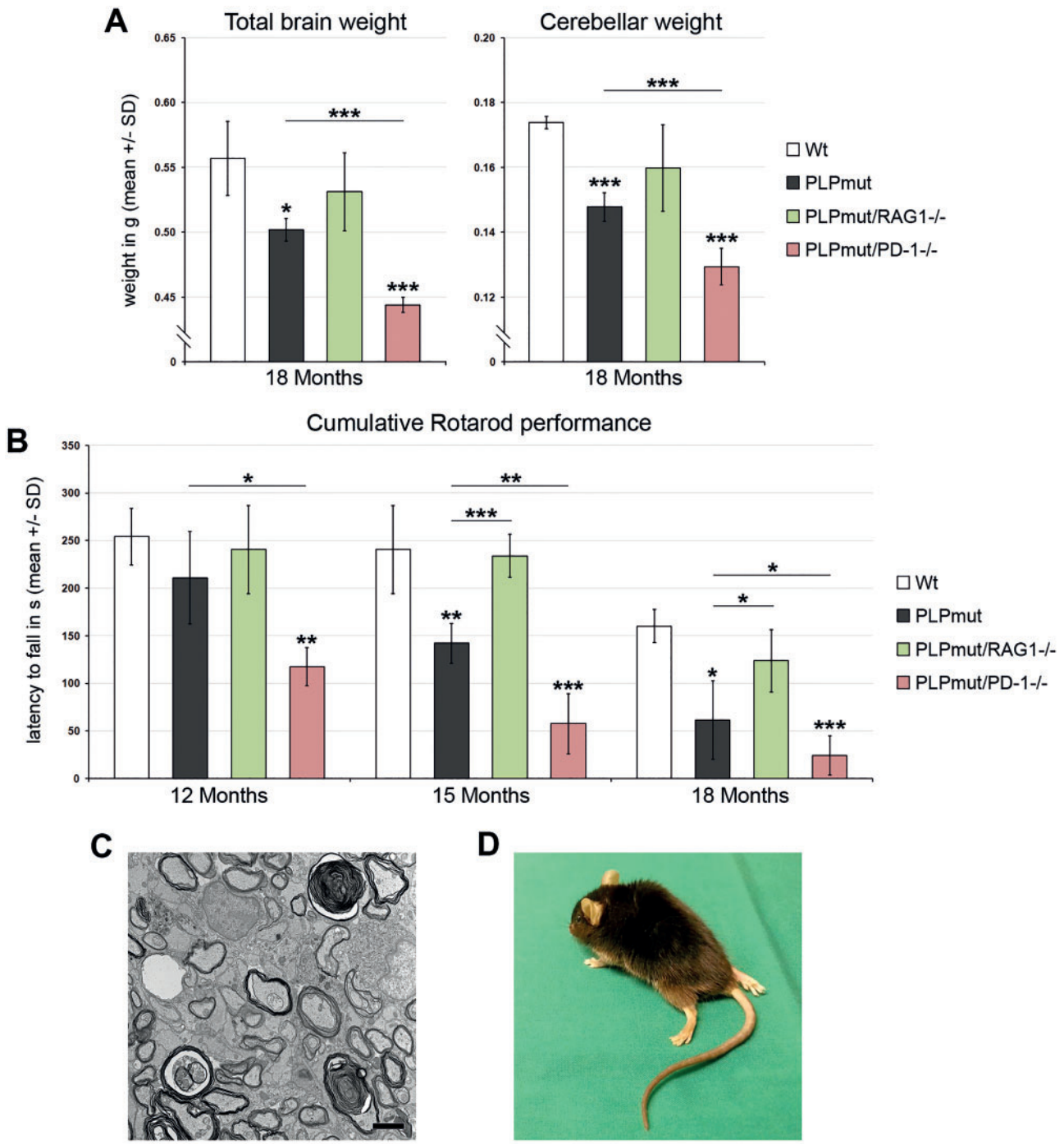

Figure 7. RAG1-deficiency attenuates and PD-1-deficiency aggravates brain atrophy and motor impairment in *PLPmut* mice. (**A**) Total brain or cerebellar atrophy was attenuated in *PLPmut/Rag1*$^{-/-}$ mice and increased in *PLPmut/Pd-1*$^{-/-}$ mice compared with *PLPmut* mice. (**B**) Longitudinal analysis of cumulative Rotarod performance at 12, 15 and 18 months of age. Motor impairment was attenuated in *PLPmut/Rag1*$^{-/-}$ mice and increased in *PLPmut/Pd-1*$^{-/-}$ mice compared with *PLPmut* mice ($n = 5$ mice per group). One-way ANOVA and Tukey's *post hoc* tests. *$P < 0.05$, **$P < 0.01$, ***$P < 0.001$. (**C**) Representative electron micrograph of an optic nerve from a *PLPmut/Pd-1*$^{-/-}$ mouse at 18 months of age. Demyelination and axonal damage (spheroids and vacuoles) were prominent. Scale bar: 2.5 μm. (**D**) Some *PLPmut/Pd-1*$^{-/-}$ mice developed hind limb paresis around 18 months of age.

Cross-breeding the transgenic mice to a *PlpKo* background was performed so that human *PLP1* mRNA was the only coding *PLP1*-related transcript present in the mice, enabling us to investigate the consequences of each individual *PLP1* mutation in detail. When investigating the corresponding protein levels by western blot analysis, a reduction by 50% in our control mice expressing the non-mutated human PLP (*hPLPWt/PlpKo*) was found compared with *Wt* mice. In this context, it is important to consider that for the generation of the mutants, we used the open reading frame of human *PLP1* cDNA so that the respective transcript lacks the potentially stabilizing and/or regulatory 3' untranslated region (3' UTR) (34,35). In accordance with the reduced protein levels, *hPLPWt/PlpKo* mice showed mild myelin abnormalities with few mild and mostly late-onset axonal

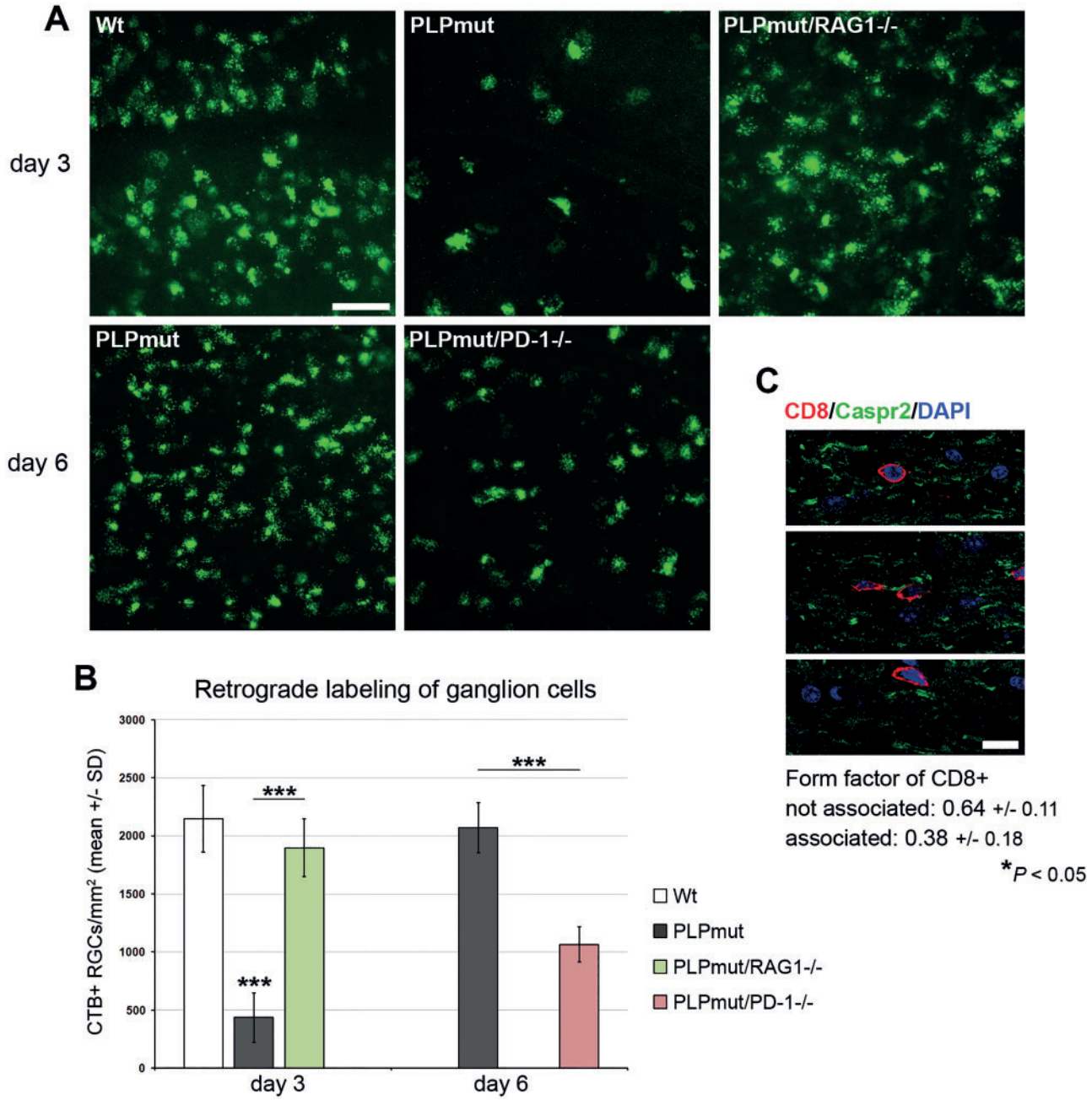

Figure 8. RAG1-deficiency attenuates and PD-1-deficiency aggravates early-onset impairment of retrograde axonal transport in *PLPmut* mice. (**A**) Representative fluorescence microscopic images of retinal flat mount preparations from 2-month-old Wt, *PLPmut*, *PLPmut/Rag1*$^{-/-}$ and *PLPmut/Pd-1*$^{-/-}$ mice at days 3 (top) and 6 (bottom) after stereotactic injections of FITC-CTB into the superior colliculi. Scale bar: 30 μm. (**B**) Quantification of FITC-CTB+ RGCs in retinal flat mount preparations. Retrograde labeling of RGCs was delayed in *PLPmut* mice compared with Wt mice ($n = 5$ mice per group). RAG1-deficiency prevented and PD-1-deficiency enhanced this delay. One-way ANOVA and Tukey's *post hoc* tests. (**C**) Representative fluorescence microscopic images of immunohistochemically labelled CD8+ T-lymphocytes (red) and Caspr2+ juxtaparanodal axonal domains (green) in longitudinal optic nerve sections from 2-month-old *PLPmut* mice ($n = 5$ mice). Scale bar: 10 μm. CD8+ T-cells that were not in close association with juxtaparanodal domains (top) showed a higher form factor (circularity) in comparison with CD8+ T-cells in close apposition with Caspr2+ juxtaparanodes (middle and bottom). Student's *t* test. $^{*}P < 0.05$, $^{***}P < 0.001$.

features. Concomitantly with these observations, neuroinflammation was low in the *hPLPWt/PlpKo* control mice.

In *hPLPW/PlpKo* mutants, there was no significant alteration in the PLP protein content in comparison to the *hPLPWt/PlpKo* mice. This was at clear variance to *hPLPG/PlpKo* mutants which displayed a substantial protein reduction in comparison to the two former mutants. Most importantly, the quantified histopathological alterations did not correlate with the respective PLP protein levels measured in the *hPLPW/PlpKo* and *hPLPG/PlpKo* mutants, as both human PLP mutations caused a common, aggravated neurodegenerative phenotype, qualitatively and quantitatively indistinguishable from genuine *PlpKo* mice. This indicates that the human mutations are functional null mutations and that dosage levels of mutant proteins are pathologically of subordinated relevance, if at all. This is in line with our observation that in both *hPLPW/PlpKo* and *hPLPG/PlpKo*

mutant mice, PLP protein was only scarcely detectable within its normal membrane destination, CNS myelin, while the bulk of the mutant protein is retained in the cell interior.

At first glance - the striking similarity between *hPLPW/PlpKo* and *hPLPG/PlpKo* on the one hand and *PlpKo* mice on the other - is unexpected. In the peripheral nervous system of mice and men, deletion of serine 63 in the *MPZ* gene causes a more severe Charcot-Marie-Tooth 1B neuropathy than the heterozygous *MPZ* null-situation (36–39) and, similar to the situation in our *PLP1* mutants, the mutant gene product is not detected in the myelin sheath, but is retained in the ER (38). Among many possibilities, one explanation for the absence of a more negative effect of intracellularly stored mutant PLP protein may be that - as opposed to Schwann cells (38) - CHOP appears to be 'beneficial' by controlling apoptosis of oligodendrocytes from *rsh* PLP-mutants, a model of Pelizaeus-Merzbacher disease (40–43).

Further studies are needed to understand the consequences of aberrant protein trafficking in our *PLP1* mutant mice accumulating mutant protein intracellularly as opposed to *PlpKo* mice lacking the protein. Additionally, it remains unknown how these processes translate to initiation of detrimental neuroinflammation and if pathways such as metabolic stress and UPR are involved (44).

Furthermore, the similarity between *hPLPW/PlpKo* and *hPLPG/PlpKo* mice and the apparent loss-of-function might be unexpected regarding the reported disease course in the respective hemizygous patients, with the 'G' mutation causing a milder phenotype than the 'W' mutation (20,21). As the 'G' mutation leads to an amino acid substitution in the PLP-specific region (as opposed to the first transmembrane 'W' mutation), in the 'G' patient (but not in our mutant mice) DM20 might compensate for the loss of PLP function in this case, similar to mice expressing DM20 only (45).

A pivotal finding was the implication of pathogenically relevant inflammatory reactions in the newly-generated *PLPmut* and the *PlpKo* mice. Interestingly, in the latter model, neuroinflammation has been observed recently, without investigating its pathogenic relevance (27). As in two other models of primarily genetically-mediated CNS diseases, comprising Pelizaeus-Merzbacher disease (14–16,18,19) and the rare lysosomal storage diseases CLN1 and CLN3 (12,13), the adaptive immune system has been demonstrated to amplify an initially milder degenerative phenotype. Surprisingly, in both the PMD and CLN models, neuroinflammation appears to aggravate predominantly axonal features, although the respective genes are not preferentially expressed in neurons: *PLP1* is predominantly glial and the CLN culprit genes *PPT1* and *CLN3* are more ubiquitously expressed. Given that axonal spheroids have been viewed as hallmarks of disturbed axon-glia interactions (26,32,46,47), our present study emphasizes the robust disease-amplifying function of the immune system when glial cells are genetically affected, as the spheroids are only scarcely seen in glial mutants that lack an intact adaptive immune system. This effect of immune-mediated amplification of pathological features is even more obvious when considering axonal transport, as its previously described perturbation (32) is only detectable in the presence of an intact adaptive immune system. Here we clearly show that, based on flat mount retina samples after injection of FITC-CTB, inactivation of the adaptive immune system rescues axonal transport completely in the *PLP1* mutants investigated. Reciprocally, reduced immune-regulation by inactivating PD-1 robustly aggravates perturbation of axonal transport and strongly increases axonal spheroid numbers, again emphasizing the impact of the adaptive immune system on axonal function and survival. Finally, using total brain/cerebellar weight and cumulative Rotarod performance as a measure for brain atrophy and clinical outcome, respectively, we found again a strong dependence of these parameters on the adaptive immune system, emphasizing the immune system as a substantial determinator of disease manifestation.

By introducing two *PLP1* mutations which cause clinical features compatible with multiple sclerosis into the genome of mice, we here clearly demonstrate the inflammation-related impact of glial perturbation. Although defined lesions, representing one histopathological feature of multiple sclerosis, are not detectable, our mutant mice share many hallmarks with PMS (3,4). In detail, we identified a diffuse and progressing neural perturbation, consisting of mild demyelination, robust axonal damage, neuronal loss and brain atrophy. A low-grade, diffuse neuroinflammation consisting of microglia/macrophage activation and elevated numbers of predominantly CD8+ T-lymphocytes in the absence of obvious BBB damage was also consistent with PMS (4). Most importantly, neuroinflammation promoted the clinically highly relevant neurodegenerative features. One subcellular target of the identified inflammation appears to be the juxtaparanode as T-lymphocytes appear to 'attack' the myelinated axons at this domain, as has been previously described in other mutants showing secondary inflammation of significant pathogenic impact (12,13,18). It has been reported that inflammation is regularly associated with the disorganization of the nodal complex and the distinct molecules typical of the respective subdomains may even serve as immunological targets (48–51). However, the role of nodal molecules as immune targets in inflammatory CNS disorders remains obscure (52).

Another interesting implication of the adaptive immune system upon experimental oligodendroglial damage has recently been demonstrated by Traka and colleagues (53). Tamoxifen-induced ablation of oligodendrocytes in PLP1-CreERT DTA mice initially lead to a reversible neurological phenotype, followed by a substantial infiltration of CD4+ T-lymphocytes, culminating in a late, fatal autoimmune reaction against MOG+ remyelinating oligodendrocytes. Although the executing pathomechanism appears to be distinct from that in our PLP1 mutant mice, both our findings and those from Traka et al. demonstrate the increasing importance of secondary inflammation in myelin-related diseases of the nervous system and support the view that MS-like disease features can be triggered by intrinsic abnormalities of oligodendrocytes.

An important issue regarding glial-related secondary inflammation is its relevance for axonal perturbation. The role of the recently proposed axo-myelinic synapse as important neuroglial compartment mediating communication between both cell types (54) might explain axonal damage when the glial cell partner is injured by likely cytotoxic immune reactions mediated by CD8+ T-lymphocytes (19). Additionally, the glial-directed immunological attack may also impair the supply of axons by oligodendrocyte-borne metabolites, such as lactate and pyruvate (55). Of note, in *PlpKo* heterozygous females, axonopathic features were almost exclusively confined to axon segments associated with myelin belonging to *Plp1* deficient oligodendrocytes, supporting our hypothesis that the immune response targets the mutant myelin sheath leading to secondary axonal perturbation (32). The previously described high vulnerability of small calibre fibres (32) can presently not be explained, but might be related to a pronounced susceptibility for immune-mediated perturbation. Further studies are needed to

investigate the functional consequences of the secondary neuroinflammation in our models and related neurological disorders.

Although some histopathological features of our mutants and the robust pathogenic role of inflammation are compatible with PMS, neuropathological features, such as progressive degeneration of preferentially long axons and clinical characteristics such as gait disturbances are also found in hereditary spastic paraplegias (HSPs). Indeed, two recent reports about SPG11 patients (56) sharing features compatible with multiple sclerosis may demonstrate overlapping pathomechanistic pathways in multiple sclerosis and some leukoencephalopathies (57,58). Another recent study describes three adolescent-onset patients carrying mutations in the aspartyl tRNA-synthetase encoding gene DARS, causing the usually early-onset hypomyelination with brainstem and spinal cord abnormalities and leg spasticity (HBSL) (59). In the context of our study it is interesting that these patients responded to steroids, again emphasizing the impact of pathogenetically-relevant neuroinflammation in a primarily genetically caused CNS disorder with robust white matter implication. This inflammatory component is so striking that the authors recommended that this genetically-mediated disorder should be included in the differential diagnosis of CNS inflammatory disorders and proposed that a steroid pulse therapy might be considered with an individualized treatment regime (59). Based on these recent reports it is unexpected that various HSP genes, including *PLP1*, are considered unlikely to have an impact on the susceptibility, clinical outcome and disease course of diagnosed multiple sclerosis (60). This latter view is supported by genome-wide association studies for multiple sclerosis as they identified predominantly immune-related genes as being multiple sclerosis-associated (61). Interestingly, a recent study using exome sequencing analysis identified *NR1H3* as a culprit gene relevant for both myelin-related lipid homeostasis and immune modulation possibly favouring neural and immunological defects as the putative cause for familiar multiple sclerosis (62).

In summary, our study shows that human mutations in a glial, HSP-related gene can cause a neurological phenotype mimicking neuroinflammatory disorders comparable to PMS. This leads to the conclusion that PMS and at least some forms of HSPs may share common final disease pathways. As many potent immunomodulatory drugs for treatment of multiple sclerosis emerged during the last years (63), and since at least some forms of HSPs might be strongly driven by neuroinflammation, it is now tempting to consider immunomodulation as a treatment option not only for PMS, but also for the so far non-treatable HSPs and possibly other genetically-mediated disorders of the nervous system accompanied by pathogenic neuroinflammation.

Materials and Methods

Generation of transgene constructs

A human *PLP1* cDNA clone (NM_000533; Open Biosystems) in Escherichia coli cultures was used for NucleoSpin plasmid preparation (Macherey-Nagel), PCR amplification for restriction site insertion and the open reading frame was subcloned into a TOPO® vector (Invitrogen) and fully sequenced (3130 Genetic Analyzer; Applied Biosystems). Single site mutagenesis was performed using the QuikChange® II XL Site-Directed Mutagenesis Kit (Stratagene) and distinct primer pairs containing the described point mutations W (20) (forward: CTTT GGGGTGGCAC**G**GTTCTGTGGCTGTGGACATG; reverse: CATG TCCACAGCCACAGAAC**C**GTGCCACCCCAAAG) or G (21) (forward: GCTCATTCTTTGGAG**T**GGGTGTGTCATTGTTTGGG; reverse: CC CAAACAATGACACACCC**A**CTCCAAAGAATGAGC). Mutant (*hPLPW*; *hPLPG*) or non-mutated (*hPLPWt*) colonies were picked, plasmid DNA was isolated, sequenced and subcloned into the pHEL*wmN1* entry vector (22) after removal of *eGFP* and *lacZ* using appropriate restriction enzymes and agarose gel extraction (Qiagen). The different entry vectors containing the transgenes were finally sequenced again.

Generation of transgenic mice, genotyping and cross-breeding

The *wmN1hsphPLP* cassettes were transferred into an HPRT Gateway destination vector by site-specific recombination using the Gateway clonase enzymes (Invitrogen). The resulting HPRT targeting vectors were transfected into B6/S-1 ES cells followed by selection for HPRT+, HAT-resistant clones. The promoter and exon I of HPRT, missing in the HPRT null ES cells, are replaced when the construct is successfully integrated by homologous recombination at the HPRT locus. A correctly targeted clone for each construct was injected into C57BL/6 blastocysts. Resulting male chimeric mice (HPRT is X-linked) were crossed to C57BL/6 females to generate F1 females bearing the transgene knocked-in on a single X chromosome.

Transgenic lines were genotyped using primers F1 (TGGCGACTACAAGACCACCATC) and R1 (ACCATACATTCTGGC ATCAGCA) to detect the *hPLP* transgenes (Supplementary Material, Fig. 1) and an additional primer pair to detect the Wt *Hprt* locus (HprtF: TTTGGCACCTGTTCGGCATGTG; HprtR: GA ATTTGCAACCTTCTTGCCTCACTG) using isolated DNA from ear punch biopsies with conventional PCR. The lines were back-crossed to a C57BL/6N genetic background. *Plp1* knockout mice were acquired from the Jackson Laboratory (Stock No: 003255), back-crossed to C57BL/6N, genotyped according to previously published protocols (25) and cross-bred with the different transgenic lines. Crossing over between the X-linked loci occurred in about 30% of offspring and enabled selection for *hPLP* transgenic mice lacking endogenous *Plp1*.

PLPmut mice were cross-bred with *Rag1*$^{-/-}$ or *Pd-1*$^{-/-}$ mice on C57BL/N genetic background according to previously published protocols (14,64).

Mice were kept in the animal facility of the Department of Neurology under barrier conditions (individually ventilated cages) and at a constant cycle of 12 h in the light (<300 lux) and 12 h in the dark. All experiments were approved by the local authority (Government of Lower Franconia, Germany).

cDNA sequencing

After rinsing the blood with PBS containing heparin, optic nerves were quickly dissected, snap frozen in liquid nitrogen, and stored at -80 °C until further processing. Nerves were homogenized (ART-MICCRA D-8, ART Labortechnik) in TRIzol reagent (Invitrogen) and total RNA was isolated according to the manufacturers' guidelines. Concentration and quality of RNA were determined using a BioPhotometer (Eppendorf) and 1 µg of RNA was reverse transcribed in a 100 µl reaction using random hexamer primers (Applied Biosystems). A cDNA region spanning the complete *hPLP* open reading frame (Supplementary Material, Fig. 1) was amplified using primers F2 (TCCGCCACC**ATG**GGCTTGTTAGAGTGC) and R2 (GCGGCCGC

TCAGAACTTGGTGCC) and the product was sequenced (3130 Genetic Analyzer; Applied Biosystems).

Semiquantitative real-time PCR (qRT-PCR)

cDNA samples were analysed as triplicates by semiquantitative real-time PCR using predeveloped TaqMan assays (Murine *Plp1*, Mm00456892_m1; Murine *Gapdh* as internal standard, Mm99999915_g1) and TaqMan universal PCR master mix (Applied Biosystems) according to the manufacturer's guidelines. Alternatively, *PLP* and/or *DM20* cDNA amplification products were analysed by SYBR Green PCR (Applied Biosystems) using *PLP* or *DM20* specific primer pairs (PLP-F: GGTTCC AGAGGCCAACATCA; PLP-R: ACCATACATTCTGGCATCAGCA; DM20-F: TGTGATCCATGCCTTCCAGT;

DM20-R: GTGATGCCCACAAACGTTGC) or densitometric quantification in the linear amplification range (using primers F1 and R1), again using murine *Gapdh* expression as internal standard.

Western blot analysis

Snap frozen optic nerves were sonicated (Sonoplus HD60, Bandelin electronic) in RIPA lysis buffer (25 mM Tris HCl pH 8, 10 mM Hepes, 150 mM NaCl, 145 mM KCl, 5 mM $MgCl_2$, 2 mM EDTA, 0.1% sodium dodecyl sulphate, 1% NP-40, 10% glycerol) containing protease inhibitors (Calbiochem). Protein concentration was determined by Lowry assay (Sigma-Aldrich) and proteins were resolved by SDS-PAGE, transferred to nitrocellulose membranes and visualized using Ponceau S (Roth). Membranes were blocked with Roti®-Block (Roth) and probed with an antibody solution overnight at 4 °C (rabbit anti-PLP, 1:5,000, abcam; mouse anti-GAPDH, 1:10,000, abcam). Incubation with horseradish peroxidase-conjugated secondary antibodies was performed for 1 h at room temperature and the detection of the immune reaction was achieved by use of ECL reagent and ECL hyperfilm (GE Healthcare).

Electron microscopy

After rinsing the blood with PBS containing heparin, mice were transcardially perfused with 4% PFA and 2% GA in cacodylate buffer. Optic nerves were dissected and post-fixed overnight in the same solution. Nerves were osmificated and processed for light and electron microscopy and morphometric quantification of neuropathological alterations was performed as previously published (12).

Histology

Retinal ganglion cells were quantified in cresyl violet stained flat mount preparations as previously described (12). For gross histology, the brains of perfused mice (4% PFA in PBS) were post-fixed overnight, olfactory bulbs and medullae were separated at defined positions and total brains or cerebella including pontes were weighed using an analytical balance (ABT 220-5DM; Kern). Brains were embedded in 6% agarose in PBS and 50 μm thick vibratome (VT1000S; Leica) sections were cut and air-dried. Sections were stained for 10 min with 2% osmium to visualize white matter regions or 0.1% cresyl violet to visualize grey matter regions, washed, dehydrated and embedded for light microscopy.

Immunohistochemistry and immunofluorescence

Freshly dissected nerves or 2% PFA-fixed and dehydrated nerves were embedded and frozen in Tissue-Tek® OCT medium (Sakura) and 10 μm thick cross- or longitudinal sections were cut using a cryostat (Leica). PLP protein expression was detected using rabbit polyclonal antibodies against PLP (1:1,000, abcam) in combination with monoclonal mouse antibodies against the mature oligodendrocyte marker APC (clone CC1; 1:100, abcam). Briefly, fresh-frozen optic nerve cross-sections were post-fixed in 4% PFA in PBS, blocked with 5% BSA and 0.3% Triton X-100 in PBS and incubated with primary antibodies in 1% BSA and 0.1% Triton X-100 overnight. Appropriate fluorescence-conjugated secondary antibodies (1:300, Dianova) were used to detect immunoreactivity and nuclei were labelled using DAPI (Sigma-Aldrich). Immunohistochemistry using antibodies against SMI32, CD11b, Sn, CD8, CD4, Albumin, Laminin and Caspr2 was performed as previously described (12–14,18). Immunopositive profiles were quantified in at least three non-adjacent sections for each animal, related to the total area of these sections and normalized to an area of 1 mm^2. Light and fluorescence microscope images were acquired using an Axiophot 2 microscope (Zeiss) with an attached CCD camera (Visitron Systems). Confocal microscopy was performed using a FluoView FV1000 (Olympus) microscope with corresponding software.

Spectral domain optical coherence tomography and funduscopy

Mice were subjected to OCT and fundus imaging with a commercially available device (Spectralis OCT; Heidelberg Engineering) and additional lenses as previously described (65). Mice were examined every 6 months for longitudinal analysis and the thickness of the innermost retinal composite layer comprising nerve fibre layer (NFL), ganglion cell layer (GCL), and inner plexiform layer (IPL) were measured in high resolution peripapillary circle scans (at least 10 measurements per scan) by an investigator unaware of the genotype of the mice. Infrared (IR) and Blue Laser Autofluorescence (BAF) fundus images were acquired at 5, 15 and 30 min after intravenous injection of 40 kDa FITC-Dextran, to monitor extravasation into the retina.

Magnetic resonance imaging

MRI was performed using a clinical 3 T unit (Magnetom Trio; Siemens) according to previously published protocols (14). The MR protocol included a T1-w inversion recovery sequence [inversion time (TI), 499 ms; repetition time (TR), 2,500 ms; echo time (TE), 14 ms; slice thickness, 0.9 mm], a T2-w turbo spin echo sequence (TR, 3,720 ms; TE, 129 ms; slice thickness, 0.7 mm) and a three-dimensional constructed interference in steady state (CISS) sequence (TR, 10.5 ms; TE, 4.88 ms; slice thickness, 0.2 mm) in the axial, coronal and sagittal planes.

Accelerating rotarod analysis

Mice were placed on a RotaRod Advanced system (TSE systems) and the time on the constantly accelerating rod (5–50 rpm; max latency: 300 s) was measured in five consecutive runs per trial. Mice were trained with two trials on 2 consecutive days and measured in a third trial on the third day. Individual runs and cumulative performance were determined at different ages in the same mice for longitudinal analysis.

Retrograde labelling of retinal ganglion cells

In order to study the retrograde axonal transport, 1.5 µl of 1% FITC-CTB (Sigma-Aldrich) in PBS were stereotactically injected into both superior colliculi of 2-month-old *PLPmut* mice and *Wt* littermates as well as RAG1- or PD-1-deficient *PLPmut* mice according to previously published protocols (12,18). Accumulation of CTB in retinal ganglion cell perikarya was quantified at day 3 and day 6 after injection in PFA-fixed flat mount preparations by fluorescence microscopy.

Experimental design and statistical analysis

All quantifications and functional/behavioural analyses were performed by investigators unaware of the genotypes of the respective mice. Only hemizygous males or homozygous females were investigated for the present study. Animals were randomly placed in experimental or control groups according to genotyping results using a random generator (http://www.randomizer.org). For biometrical sample size estimation, the program G*Power (version 3.1.3) was used (Heinrich Heine University Duesseldorf). Calculation of appropriate sample size groups was performed in *a priori* power analysis by comparing the mean of two groups with a defined adequate power of 0.8 (1 - β-error) and an α-error of 0.05. To determine the pre-specified effect size *d*, previously published data were considered as comparable reference values (12). Statistical analysis was performed using PASW Statistics 18 (SPSS, IBM) software. Shapiro-Wilk test was used to check for normal distribution of data. Parametric comparisons between values of age-matched *Wt* mice and *PLPmut* mice were made by unpaired two-tailed Student's *t*-test.

Nonparametric statistical analyses of data were performed by use of the Mann-Whitney *U*-test. For multiple comparisons, one-way ANOVA followed by Tukey's *post hoc* tests or Kruskal-Wallis tests with Bonferroni correction were applied. *P* values considered as significant were indicated by asterisks according to the following scheme: $^{*}P < 0.05$; $^{**}P < 0.01$; $^{***}P < 0.001$. Significant differences of a respective genotype group in comparison with *Wt* mice are indicated above the corresponding bar.

Supplementary Material

Supplementary Material is available at *HMG* online.

Acknowledgements

The authors are grateful to Klaus-Armin Nave (Göttingen) and Mark P. Gorman (Boston, USA) for helpful discussions. We thank Heinrich Blazyca, Silke Loserth, and Bettina Meyer for expert technical assistance, and Helga Brünner, Jacqueline Schreiber, Anja Weidner, and Jennifer Bauer for attentive care of mice.

Conflict of Interest statement. None declared.

Funding

This work received major support by the Roman, Marga and Mareille Sobek-Foundation (Research award to R.M.), by the German Research Foundation (SFB 581, to R.M. and M.S.) and by the Interdisciplinary Centre for Clinical Research (IZKF) of the University of Wuerzburg (A-168, to R.M. and M. B.). Supplementary support was provided by a recent grant from the Gemeinnützige Hertie Stiftung (P1150084, to J.G.).

References

1. Trapp, B.D. and Nave, K.A. (2008) Multiple sclerosis: an immune or neurodegenerative disorder?. *Annu. Rev. Neurosci.*, **31**, 247–269.
2. Lassmann, H. (2013) Pathology and disease mechanisms in different stages of multiple sclerosis. *J. Neurol. Sci.*, **333**, 1–4.
3. Koch, M.W., Cutter, G., Stys, P.K., Yong, V.W. and Metz, L.M. (2013) Treatment trials in progressive MS-current challenges and future directions. *Nat. Rev. Neurol.*, **9**, 496–503.
4. Lassmann, H., van Horssen, J. and Mahad, D. (2012) Progressive multiple sclerosis: pathology and pathogenesis. *Nat. Rev. Neurol.*, **8**, 647–656.
5. Stys, P.K., Zamponi, G.W., van Minnen, J. and Geurts, J.J. (2012) Will the real multiple sclerosis please stand up?. *Nat. Rev. Neurosci.*, **13**, 507–514.
6. Stys, P.K. (2013) Pathoetiology of multiple sclerosis: are we barking up the wrong tree?. *F1000Prime Rep.*, **5**, 20.
7. Glass, C.K., Saijo, K., Winner, B., Marchetto, M.C. and Gage, F.H. (2010) Mechanisms underlying inflammation in neurodegeneration. *Cell*, **140**, 918–934.
8. Hirsch, E.C. and Hunot, S. (2009) Neuroinflammation in Parkinson's disease: a target for neuroprotection?. *Lancet Neurol.*, **8**, 382–397.
9. Nguyen, M.D., D'Aigle, T., Gowing, G., Julien, J.P. and Rivest, S. (2004) Exacerbation of motor neuron disease by chronic stimulation of innate immunity in a mouse model of amyotrophic lateral sclerosis. *J. Neurosci.*, **24**, 1340–1349.
10. Gomez-Nicola, D., Fransen, N.L., Suzzi, S. and Perry, V.H. (2013) Regulation of microglial proliferation during chronic neurodegeneration. *J. Neurosci.*, **33**, 2481–2493.
11. Gill, D. and Veltkamp, R. (2016) Dynamics of T cell responses after stroke. *Curr. Opin. Pharmacol.*, **26**, 26–32.
12. Groh, J., Kuhl, T.G., Ip, C.W., Nelvagal, H.R., Sri, S., Duckett, S., Mirza, M., Langmann, T., Cooper, J.D. and Martini, R. (2013) Immune cells perturb axons and impair neuronal survival in a mouse model of infantile neuronal ceroid lipofuscinosis. *Brain*, **136**, 1083–1101.
13. Groh, J., Ribechini, E., Stadler, D., Schilling, T., Lutz, M.B. and Martini, R. (2016) Sialoadhesin promotes neuro inflammation-related disease progression in two mouse models of CLN disease. *Glia*, **64**, 792–809.
14. Ip, C.W., Kroner, A., Bendszus, M., Leder, C., Kobsar, I., Fischer, S., Wiendl, H., Nave, K.A. and Martini, R. (2006) Immune cells contribute to myelin degeneration and axonopathic changes in mice overexpressing proteolipid protein in oligodendrocytes. *J. Neurosci.*, **26**, 8206–8216.
15. Ip, C.W., Kroner, A., Crocker, P.R., Nave, K.A. and Martini, R. (2007) Sialoadhesin deficiency ameliorates myelin degeneration and axonopathic changes in the CNS of PLP overexpressing mice. *Neurobiol. Dis.*, **25**, 105–111.
16. Kroner, A., Schwab, N., Ip, C.W., Leder, C., Nave, K.A., Maurer, M., Wiendl, H. and Martini, R. (2009) PD-1 regulates neural damage in oligodendroglia-induced inflammation. *Plos One*, **4**, e4405.
17. Ip, C.W., Kohl, B., Kleinschnitz, C., Reuss, B., Nave, K.A., Kroner, A. and Martini, R. (2008) Origin of CD11b+ macrophage-like cells in the CNS of PLP-overexpressing mice: low influx of haematogenous macrophages and unchanged blood-brain-barrier in the optic nerve. *Mol. Cell. Neurosci.*, **38**, 489–494.
18. Ip, C.W., Kroner, A., Groh, J., Huber, M., Klein, D., Spahn, I., Diem, R., Williams, S.K., Nave, K.A., Edgar, J.M., *et al.* (2012) Neuroinflammation by cytotoxic T-lymphocytes impairs

retrograde axonal transport in an oligodendrocyte mutant mouse. *Plos One*, **7**, e42554.
19. Kroner, A., Ip, C.W., Thalhammer, J., Nave, K.A. and Martini, R. (2010) Ectopic T-cell specificity and absence of perforin and granzyme B alleviate neural damage in oligodendrocyte mutant mice. *Am. J. Pathol.*, **176**, 549–555.
20. Warshawsky, I., Rudick, R.A., Staugaitis, S.M. and Natowicz, M.R. (2005) Primary progressive multiple sclerosis as a phenotype of a PLP1 gene mutation. *Ann. Neurol.*, **58**, 470–473.
21. Gorman, M.P., Golomb, M.R., Walsh, L.E., Hobson, G.M., Garbern, J.Y., Kinkel, R.P., Darras, B.T., Urion, D.K. and Eksioglu, Y.Z. (2007) Steroid-responsive neurologic relapses in a child with a proteolipid protein-1 mutation. *Neurology*, **68**, 1305–1307.
22. Tuason, M.C., Rastikerdar, A., Kuhlmann, T., Goujet-Zalc, C., Zalc, B., Dib, S., Friedman, H. and Peterson, A. (2008) Separate proteolipid protein/DM20 enhancers serve different lineages and stages of development. *J. Neurosci.*, **28**, 6895–6903.
23. Bronson, S.K., Plaehn, E.G., Kluckman, K.D., Hagaman, J.R., Maeda, N. and Smithies, O. (1996) Single-copy transgenic mice with chosen-site integration. *Proc. Natl. Acad. Sci. USA*, **93**, 9067–9072.
24. Farhadi, H.F., Lepage, P., Forghani, R., Friedman, H.C., Orfali, W., Jasmin, L., Miller, W., Hudson, T.J. and Peterson, A.C. (2003) A combinatorial network of evolutionarily conserved myelin basic protein regulatory sequences confers distinct glial-specific phenotypes. *J. Neurosci.*, **23**, 10214–10223.
25. Klugmann, M., Schwab, M.H., Pühlhofer, A., Schneider, A., Zimmermann, F., Griffiths, I.R. and Nave, K.A. (1997) Assembly of CNS myelin in the absence of proteolipid protein. *Neuron*, **18**, 59–70.
26. Griffiths, I., Klugmann, M., Anderson, T., Yool, D., Thomson, C., Schwab, M.H., Schneider, A., Zimmermann, F., McCulloch, M., Nadon, N., *et al.* (1998) Axonal swellings and degeneration in mice lacking the major proteolipid of myelin. *Science*, **280**, 1610–1613.
27. de Monasterio-Schrader, P., Patzig, J., Mobius, W., Barrette, B., Wagner, T.L., Kusch, K., Edgar, J.M., Brophy, P.J. and Werner, H.B. (2013) Uncoupling of neuroinflammation from axonal degeneration in mice lacking the myelin protein tetraspanin-2. *Glia*, **61**, 1832–1847.
28. Harlow, D.E., Saul, K.E., Culp, C.M., Vesely, E.M. and Macklin, W.B. (2014) Expression of proteolipid protein gene in spinal cord stem cells and early oligodendrocyte progenitor cells is dispensable for normal cell migration and myelination. *J. Neurosci.*, **34**, 1333–1343.
29. Petit, B., Giraudet, F., Bechon, C., Bardin, L., Avan, P., Boespflug-Tanguy, O. and Begou, M. (2014) Mice with a deletion of the major central myelin protein exhibit hypersensitivity to noxious thermal stimuli: involvement of central sensitization. *Neurobiol. Dis.*, **65**, 55–68.
30. Yool, D.A., Klugmann, M., McLaughlin, M., Vouyiouklis, D.A., Dimou, L., Barrie, J.A., McCulloch, M.C., Nave, K.A. and Griffiths, I.R. (2001) Myelin proteolipid proteins promote the interaction of oligodendrocytes and axons. *J. Neurosci. Res.*, **63**, 151–164.
31. Mombaerts, P., Iacomini, J., Johnson, R.S., Herrup, K., Tonegawa, S. and Papaioannou, V.E. (1992) RAG-1-deficient mice have no mature B and T lymphocytes. *Cell*, **68**, 869–877.
32. Edgar, J.M., McLaughlin, M., Yool, D., Zhang, S.C., Fowler, J.H., Montague, P., Barrie, J.A., McCulloch, M.C., Duncan, I.D., Garbern, J., *et al.* (2004) Oligodendroglial modulation of fast axonal transport in a mouse model of hereditary spastic paraplegia. *J. Cell Biol.*, **166**, 121–131.
33. Readhead, C., Schneider, A., Griffiths, I. and Nave, K.A. (1994) Premature arrest of myelin formation in transgenic mice with increased proteolipid protein gene dosage. *Neuron*, **12**, 583–595.
34. Mallon, B.S. and Macklin, W.B. (2002) Overexpression of the 3'-untranslated region of myelin proteolipid protein mRNA leads to reduced expression of endogenous proteolipid mRNA. *Neurochem. Res.*, **27**, 1349–1360.
35. Wang, E. and Cambi, F. (2012) MicroRNA expression in mouse oligodendrocytes and regulation of proteolipid protein gene expression. *J. Neurosci. Res.*, **90**, 1701–1712.
36. Kulkens, T., Bolhuis, P.A., Wolterman, R.A., Kemp, S., te Nijenhuis, S., Valentijn, L.J., Hensels, G.W., Jennekens, F.G.I., de Visser, M., Hoogendijk, J.E., *et al.* (1993) Deletion of the serine 34 codon from the major peripheral myelin protein P0 gene in Charcot-Marie-Tooth disease type 1B. *Nat. Genet.*, **5**, 35–39.
37. Warner, L.E., Hilz, M.J., Appel, S.H., Killian, J.M., Kolodny, E.H., Karpati, G., Carpenter, S., Watters, G.V., Wheeler, C., Witt, D., *et al.* (1996) Clinical phenotypes of different MPZ (P0) mutations may include Charcot-Marie-Tooth 1B, Dejerine-Sottas, and congenital hypomyelination. *Neuron*, **17**, 451–460.
38. Pennuto, M., Tinelli, E., Malaguti, M., Del Carro, U., D'Antonio, M., Ron, D., Quattrini, A., Feltri, M.L. and Wrabetz, L. (2008) Ablation of the UPR-Mediator CHOP Restores Motor Function and Reduces Demyelination in Charcot-Marie-Tooth 1B Mice. *Neuron*, **57**, 393–405.
39. Martini, R., Zielasek, J., Toyka, K.V., Giese, K.P. and Schachner, M. (1995) Protein zero (P0)-deficient mice show myelin degeneration in peripheral nerves characteristic of inherited human neuropathies. *Nat. Genet.*, **11**, 281–286.
40. Southwood, C.M., Garbern, J., Jiang, W. and Gow, A. (2002) The unfolded protein response modulates disease severity in Pelizaeus-Merzbacher disease. *Neuron*, **36**, 585–596.
41. Gow, A. and Wrabetz, L. (2009) CHOP and the endoplasmic reticulum stress response in myelinating glia. *Curr. Opin. Neurobiol.*, **19**, 505–510.
42. D'Antonio, M., Musner, N., Scapin, C., Ungaro, D., Del Carro, U., Ron, D., Feltri, M.L. and Wrabetz, L. (2013) Resetting translational homeostasis restores myelination in Charcot-Marie-Tooth disease type 1B mice. *J. Exp. Med.*, **210**, 821–838.
43. Clayton, B.L. and Popko, B. (2016) Endoplasmic reticulum stress and the unfolded protein response in disorders of myelinating glia. *Brain Res.*, doi:10.1016/j.brainres.2016.03.046.
44. Southwood, C.M., Fykkolodziej, B., Dachet, F. and Gow, A. (2013) Potential For Cell-mediated Immune Responses In Mouse Models Of Pelizaeus-Merzbacher Disease. *Brain Sci.*, **3**, 1417–1444.
45. Sporkel, O., Uschkureit, T., Bussow, H. and Stoffel, W. (2002) Oligodendrocytes expressing exclusively the DM20 isoform of the proteolipid protein gene: myelination and development. *Glia*, **37**, 19–30.
46. Nave, K.A. (2010) Myelination and support of axonal integrity by glia. *Nature*, **468**, 244–252.
47. Nave, K.A. (2010) Myelination and the trophic support of long axons. *Nat. Rev. Neurosci.*, **11**, 275–283.
48. Derfuss, T., Linington, C., Hohlfeld, R. and Meinl, E. (2010) Axo-glial antigens as targets in multiple sclerosis: implications for axonal and grey matter injury. *J. Mol. Med.*, **88**, 753–761.
49. Dhaunchak, A.S., Becker, C., Schulman, H., De Faria, O., Jr., Rajasekharan, S., Banwell, B., Colman, D.R. and Bar-Or, A.

(2012) Implication of perturbed axoglial apparatus in early pediatric multiple sclerosis. *Ann. Neurol.*, **71**, 601–613.
50. Zoupi, L., Markoullis, K., Kleopa, K.A. and Karagogeos, D. (2013) Alterations of juxtaparanodal domains in two rodent models of CNS demyelination. *Glia*, **61**, 1236–1249.
51. Stathopoulos, P., Alexopoulos, H. and Dalakas, M.C. (2015) Autoimmune antigenic targets at the node of Ranvier in demyelinating disorders. *Nat. Rev. Neurol.*, **11**, 143–156.
52. Hohlfeld, R., Dornmair, K., Meinl, E. and Wekerle, H. (2016) The search for the target antigens of multiple sclerosis, part 2: CD8+ T cells, B cells, and antibodies in the focus of reverse-translational research. *Lancet Neurol.*, **15**, 317–331.
53. Traka, M., Podojil, J.R., McCarthy, D.P., Miller, S.D. and Popko, B. (2016) Oligodendrocyte death results in immune-mediated CNS demyelination. *Nat. Neurosci.*, **19**, 65–74.
54. Micu, I., Plemel, J.R., Lachance, C., Proft, J., Jansen, A.J., Cummins, K., van Minnen, J. and Stys, P.K. (2016) The molecular physiology of the axo-myelinic synapse. *Exp. Neurol.*, **276**, 41–50.
55. Fünfschilling, U., Supplie, L.M., Mahad, D., Boretius, S., Saab, A.S., Edgar, J., Brinkmann, B.G., Kassmann, C.M., Tzvetanova, I.D., Mobius, W., *et al.* (2012) Glycolytic oligodendrocytes maintain myelin and long-term axonal integrity. *Nature*, **485**, 517–521.
56. Stevanin, G., Santorelli, F.M., Azzedine, H., Coutinho, P., Chomilier, J., Denora, P.S., Martin, E., Ouvrard-Hernandez, A.M., Tessa, A., Bouslam, N., *et al.* (2007) Mutations in SPG11, encoding spatacsin, are a major cause of spastic paraplegia with thin corpus callosum. *Nat. Genet.*, **39**, 366–372.
57. Romagnolo, A., Masera, S., Mattioda, A., Superti, G., Santorelli, F.M., Mongini, T., Pinessi, L. and Cavalla, P. (2014) Atypical hereditary spastic paraplegia mimicking multiple sclerosis associated with a novel SPG11 mutation. *Eur. J. Neurol.*, **21**, e14–e15.
58. Laurencin, C., Rascle, L., Cotton, F., Grosset-Janin, C., Bernard, E., Depienne, C., Vukusic, S. and Thobois, S. (2016) A rare case of SPG11 mutation with multiple sclerosis. *Rev. Neurol. (Paris)*, **172**, 389–391.
59. Wolf, N.I., Toro, C., Kister, I., Latif, K.A., Leventer, R., Pizzino, A., Simons, C., Abbink, T.E., Taft, R.J., van der Knaap, M.S., *et al.* (2015) DARS-associated leukoencephalopathy can mimic a steroid-responsive neuroinflammatory disorder. *Neurology*, **84**, 226–230.
60. DeLuca, G.C., Ramagopalan, S.V., Cader, M.Z., Dyment, D.A., Herrera, B.M., Orton, S., Degenhardt, A., Pugliatti, M., Sadovnick, A.D., Sotgiu, S., *et al.* (2007) The role of hereditary spastic paraplegia related genes in multiple sclerosis. A study of disease susceptibility and clinical outcome. *J. Neurol.*, **254**, 1221–1226.
61. Bashinskaya, V.V., Kulakova, O.G., Boyko, A.N., Favorov, A.V. and Favorova, O.O. (2015) A review of genome-wide association studies for multiple sclerosis: classical and hypothesis-driven approaches. *Hum. Genet.*, **134**, 1143–1162.
62. Wang, Z., Sadovnick, A.D., Traboulsee, A.L., Ross, J.P., Bernales, C.Q., Encarnacion, M., Yee, I.M., de Lemos, M., Greenwood, T., Lee, J.D., *et al.* (2016) Nuclear Receptor NR1H3 in Familial Multiple Sclerosis. *Neuron*, **90**, 948–954.
63. Curtin, F. and Hartung, H.P. (2014) Novel therapeutic options for multiple sclerosis. *Expert Rev. Clin. Pharmacol.*, **7**, 91–104.
64. Kroner, A., Schwab, N., Ip, C.W., Sommer, C., Wessig, C., Wiendl, H. and Martini, R. (2009) The co-inhibitory molecule PD-1 modulates disease severity in a model for an inherited, demyelinating neuropathy. *Neurobiol. Dis.*, **33**, 96–103.
65. Groh, J., Stadler, D., Buttmann, M. and Martini, R. (2014) Non-invasive assessment of retinal alterations in mouse models of infantile and juvenile neuronal ceroid lipofuscinosis by spectral domain optical coherence tomography. *Acta Neuropathol. Commun.*, **2**, 54.